Spontaneous driving forces give rise to protein-RNA condensates with coexisting phases and complex material properties

Steven Boeynaems[1,*], Alex S. Holehouse[2], Venera Weinhardt[3,4], Denes Kovacs[5], Joris Van Lindt[5], Carolyn Larabell[3,4], Ludo Van Den Bosch[6,7], Rhiju Das[8], Peter S. Tompa[5,9], Rohit V. Pappu[2,*], and Aaron D. Gitler[1,*]

1. Department of Genetics, Stanford University School of Medicine, Stanford, California 94305, USA
2. Department of Biomedical Engineering & Center for Biological Systems Engineering, Washington University, St. Louis, Missouri 63130, USA
3. Molecular Biophysics and Integrated Bioimaging Division, Lawrence Berkeley National Laboratory, Berkeley, California, USA
4. Department of Anatomy, University of California San Francisco, San Francisco, California, USA
5. VIB, Center for Structural Biology (CSB), Vrije Universiteit Brussel (VUB), Brussels, Belgium
6. VIB, Center for Brain & Disease Research, Laboratory of Neurobiology, Leuven, Belgium
7. KU Leuven, Department of Neurosciences, Experimental Neurology, Leuven, Belgium
8. Departments of Biochemistry and Physics, Stanford University, Stanford, California 94305, USA
9. Institute of Enzymology, Research Centre for Natural Sciences of the Hungarian Academy of Sciences, Budapest, Hungary

***Corresponding authors:**
Steven Boeynaems
E-mail: sboeynae@stanford.edu

Rohit V. Pappu
E-mail: pappu@wustl.edu

Aaron D. Gitler
E-mail: agitler@stanford.edu

KEYWORDS

Phase transitions, biomolecular condensates, complex coacervation, RNA, intrinsically disordered proteins, and Arginine-rich domains

SIGNIFICANCE STATEMENT

Biomolecular condensates comprise of multiple protein and RNA molecules that are organized into complex mesoscale morphologies. Does it always take active, energy-dependent processes to form complex morphologies or can spontaneous processes yield condensates that mimic morphologies observed in cells? Here, we answer this question using a panel of systematic *in vitro* studies directed at biologically relevant low complexity protein sequences and a set of homopolymeric RNA molecules. We find that coexisting liquid- and solid-like material properties and multilayered architectures result from sequence-encoded driving forces that control the spontaneous formation of protein and RNA condensates. Our studies suggest that spontaneous processes are likely to be central for forming and regulating condensates *in vivo*.

ABSTRACT

Collective phase transitions, including phase separation and gelation of multivalent protein and RNA molecules appears to underlie the biogenesis of biomolecular condensates such as membraneless organelles. *In vivo*, these condensates encompass hundreds of distinct types of molecules that are often organized into multi-layered structures supporting the differential partitioning of molecules into distinct regions with distinct material properties. The interplay between driven (active) versus spontaneous (passive) processes that are required for enabling the formation of condensates with coexisting layers of distinct material properties remains unclear. Here, we investigate the role of spontaneous driving forces as determinants of protein-RNA condensates with complex morphologies and distinct material properties. Through the use of systematic *in vitro* experiments and simulations based on coarse-grained models we find that that the collective interactions among the simplest, biologically relevant proteins and archetypal RNA molecules are sufficient for driving the spontaneous emergence of multi-layered condensates with distinct material properties. Our results demonstrate that key properties of protein-RNA condensates such as their overall morphologies, internal dynamics, and the selective partitioning of substrates are governed specific amino acid chemistries as well as RNA sequence and secondary structure. Our findings yield a clear set of heuristics regarding homo- and heterotypic interactions that are likely to be relevant for understanding the interplay between active and passive processes that control the formation of functional biomolecular condensates.

INTRODUCTION

Phase transitions of protein and RNA molecules are implicated as drivers of spatial and temporal organization of cellular matter (1-3). The relevant phase transitions include first-order transitions such as phase separation and higher-order transitions such as sol-gel transitions (4, 5). These phase transitions are thought to be drivers of the biogenesis of membraneless organelles and other non-stoichiometric assemblies that are collectively referred to as *biomolecular condensates* (4, 6, 7). Key protein and RNA molecules, referred to as scaffolds, are found to be necessary and sufficient to drive phase separation *in vitro* (1-3). However, transferring insights from *in vitro* studies to an understanding of *in vivo* condensates requires an understanding of the interplay between driven (active) and spontaneous (passive) processes (2, 4, 8).

Several *in vivo* observations regarding condensates are thought to involve active processes that incur the expenditure of energy while maintaining condensates in metastable states (2). Relevant observations include the determinants of material properties, inhibition of aging and fusion of condensates, the selective partitioning or extraction of molecular components, the dissolution of condensates, and the maintenance of spatially organized structures within condensates. For example, stress granules are cytoplasmic RNA-protein granules that form when cells are under stress and disassemble when the stresses abate (9, 10). Their functions / dysfunctions have been implicated in viral infections, cancers, and neurodegenerative disorders (11-16). Data from mammalian cells suggests that these granules consist of dense solid-like cores of RNA and proteins surrounded by a labile liquid shell (17, 18). Similarly, the nucleolus consists of three discrete layers and each layer is characterized by distinct inward and outward fluxes of protein and RNA molecules. Recent work suggests that the multi-layered topology of nucleoli could arise through differences in surface tensions associated with the distinct liquid phases (19). Indeed it appears that many spatially organized structures can arise through spontaneous processes alone (20, 21). In contrast, *in vivo* regulation and dissolution of these architectures, as opposed to their formation, might require the intervention of active processes (22). For example, the layered topology of nucleoli is reversed during transcriptional inhibition, suggesting that additional molecular interactions might be involved in nucleolar regulation (23).

The majority of known biomolecular condensates contain multiple protein and RNA molecules. Even condensates that are not directly involved in RNA metabolism or harbor canonical RNA binding proteins seem to contain or even require RNA for their formation. For example, G-bodies are reversible assemblies of glycolytic enzymes that form under hypoxia (24). Not only do these condensates stain positively for specific RNA molecules, the treatment of cells with nucleases results in the dissociation of G-bodies thus suggesting a role for RNA molecules as scaffolds that drive the formation of these bodies (24). Recent studies suggest that RNA molecules undergo conformational transitions such as chain compaction in the context of stress granules. This is to be contrasted with the expanded conformations formed by the same RNA molecules in the cytosol (25). Indeed, roughly 10^3 RNA species are preferentially associated with stress granules, and these RNAs are enriched for specific sequence and structural features (26, 27). RNA molecules also have the ability to undergo phase separation even in the absence of protein partners (28). RNA phase separation appears to underlie repeat RNA foci formation in repeat expansion disorders (29). Additionally, RNA also controls the dynamic properties of RNA transport granules (30) and nucleoli (31, 32), implying that RNA molecules also regulate the material properties of condensed phases. To what extent could spontaneous processes governed by sequence-intrinsic properties of protein and RNA sequences explain *in vivo* observations? In this work, we address this question by investigating the chemical and structural determinants of spontaneous processes governed by the interactions amongst chemically simple yet biologically relevant proteins and archetypal RNA molecules.

We deployed *in vitro* model systems for phase separation that were designed to uncover the rules governing RNA and protein-driven interactions. For the protein system, we used intrinsically disordered arginine-rich and lysine-rich dipeptide repeat sequences (33). We investigated the interplay between these polypeptides and a series of homopolymeric RNA sequences. Our results show that purine versus pyrimidine contents of RNA molecules directly influence condensate morphology and dynamics. We trace these effects to the details of RNA sequence and the affinities of protein-RNA interactions. Strikingly, the differences in molecular specificities of protein-protein, protein-RNA, and RNA-RNA interactions lead to the spontaneous generation of spatially organized condensates with sub-compartments, thus providing insights regarding spontaneous, sequence-encoded driving forces for condensates with complex architectures and dynamics.

RESULTS

Polyanions determine material properties of arginine-based protein phase separation: Arginine-rich, intrinsically disordered, low complexity domains have been established as key regions that drive protein phase separation *in vitro* and *in vivo* (33-41). Previous studies quantified the phase behavior driven by two types of toxic arginine-rich dipeptide repeats that are generated by aberrant translation of a hexanucleotide repeat expansion in the *C9orf72* gene, the major genetic cause underlying amyotrophic lateral sclerosis (ALS) (42-44). Protein products of these repeats include poly(proline-arginine) and poly(glycine-arginine), which we refer to hereafter as PR and GR, respectively. These proteins target and perturb various condensates, including the nucleolus and stress granules (33-35). Mechanistic studies of PR phase separation *in vitro* revealed that phase separation of arginine-rich systems is driven by a combination of electrostatic interactions, and interactions involving pi systems (33, 45).

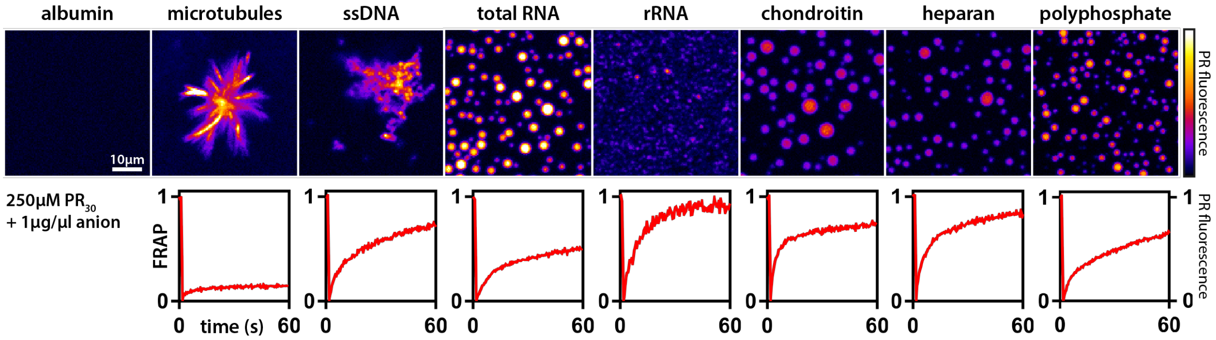

Figure 1: Morphologies and dynamics of condensates formed via complex coacervation of PR$_{30}$ are governed by the chemistry of polyanions. Each panel in the top row shows PR$_{30}$ (PR) fluorescence in the context of condensates formed by complex coacervation. All measurements were performed in the presence of 250 µM of PR$_{30}$ and 1 µg/µL of polyanion. Under these conditions, albumin, a generic protein macro-anion does not promote phase separation. However, all other polyanions in the current study promote phase separation, although the morphologies of the condensates are specific to the type of polyanion used to drive phase separation. The bottom row shows normalized kinetic traces from FRAP experiments. In each of the experiments, the fluorescently labeled PR$_{30}$ molecules are photobleached and the recovery of fluorescence is monitored as a function of time. FRAP dynamics of PR$_{30}$ molecules exhibit a clear dependence on polyanions. Visual inspection reveals a correlation between spherical morphologies and rapid recovery of fluorescence.

Phase separation driven by interactions among complexing polyions is known as complex coacervation (46). We examined PR-mediated phase separation via complex coacervation using a wide array of biological polyanions. Whereas albumin, a negatively charged protein, could not induce phase separation, long polyanions or negatively charged protein assemblies robustly drive either assembly formation or PR recruitment (**Figure 1**). The morphologies of the resulting condensates were dependent on the specific type of polyanion and their assembly state: Microtubule asters or filaments provided a solid scaffold for PR recruitment, while flexible polyanions such as total yeast RNA or polyphosphate lead to the formation of spherical droplets, indicative of a minimization of surface tension that is consistent with liquid-liquid phase separation driven by complex coacervation (47). Additionally, although the same PR$_{30}$ polycation was used in all cases, we observed substantially different PR dynamics within condensates that depends on the polyanion in question, as assayed by fluorescence recovery after photobleaching (FRAP). These results indicate that the chemical and structural details of the complexing polyanions are important determinants of the material properties associated with protein-polyanion assemblies. Furthermore, our results support a model in which the details of complex coacervation are influenced by the chemical identity of the constituent cations and anions within polycations and polyanions, respectively. It would appear that a combination of generic and specific driving forces could be involved in the formation of condensates via complex coacervation.

RNA structure determines protein coacervate morphology: To uncover the physico-chemical determinants of generic versus specific driving forces in complex coacervation involving protein and RNA molecules, we focused our attention on elucidating the rules associated with complex coacervation of PR as influenced by different types of homopolymeric RNA molecules. Mixing PR_{30} with homopolymeric RNAs (Mw = 600-1,000 kDa) (37) leads to the spontaneous formation of condensates at room temperature. As can be seen in **Figure 2A-B** (and **Movie S1**), mixing of PR with homopolymeric RNAs (except poly-rG) results in the formation of liquid-like condensates. We make this assessment based on the spherical shapes of the assemblies, the wetting of glass surfaces, and the fusion of condensates. Poly-rA, poly-rC, and poly-rU are unlikely to form persistent higher-order (tertiary) structure, although there is evidence that intramolecular base stacking can drive the formation of short helical regions interspersed by random-coil like segments (48). In contrast, poly-rG forms G-quadruplexes and these structural elements are highly stable (49). Interestingly, unlike the spherical coacervates formed by complexation of each of poly-rA, poly-rC, and poly-rU with PR, the assemblies formed by poly-rG and PR peptides are characterized by an open, fractal-like network structure. The morphologies we observe for the assemblies of PR and poly-rG are concordant with kinetically arrested phase separation leading to the formation of gels. A deep quench into the two-phase regime can give rise to continuous transitions such as sol-gel transitions, which are a manifestation of kinetically arrested phase separation (50). Interestingly, however, the PR molecules within open networked structures retain their dynamical properties, indicating that the non-covalent physical crosslinks among PR - poly-rG molecules are labile on the timescale of the experiments (*SI Appendix* **Figure S1A, Figure S2D**). The addition of RNA molecules such as poly-rC, which makes complementary base pairing interactions with poly-rG, reduces the formation of these open networks. This reduction occurs in a dose-dependent manner and is indicative of competitive formation of structures that displace G-quadruplex formation (*SI Appendix* **Figure S1A-C, Movie S2**).

To further test the impact of stable RNA structures as determinants of condensate morphology, we combined base pairing and non-base pairing RNA species prior to induction of PR phase separation (**Figure 2C**). Combining poly-rA and poly-rU (poly-rA:rU), but not poly-rA-poly-rC or poly-rU-poly-rC, resulted in the formation of large granular and filament / sheet-like assemblies. A detailed three-dimensional view of the interconnected network formed by the base pairing RNAs can be seen in **Figure 2E** (**Movie S3**), as visualized using soft x-ray tomography (SXT). Interestingly, when pre-formed PR-poly-rA and PR-poly-rU condensates were mixed together we did not observe the formation of filamentous structures. Instead, small spherical assemblies are observed (*SI Appendix* **Figure S1E**). This observation suggests that RNA base pairing arrests complex coacervation of RNA and PR molecules by sequestering the RNA molecules into stable base paired structures that are able to incorporate PR molecules in a manner that does not disrupt base-pairing interactions (i.e., through interactions with the phosphate backbone) (51). Therefore, it appears plausible that at least one of the two phases observed for mixtures of poly-rA + poly-rU + PR is a metastable phase. Given that base pairing appears to drive extended network formation, we reasoned that interfering with base pairing should disrupt the formation of networked structures and promote phase separation. Urea is known to destabilize protein and RNA structure (52). Addition of urea to open network assemblies helped prevent the formation of networked structures, but this did not result in droplet formation (**Figure 2D**). However, thermal denaturation of the poly-rA:rU-PR assemblies followed by an annealing reaction helped convert pre-formed open networks into spherical assemblies. This is suggestive of a disruption of metastable, networked structures and an annealing reaction that yields the thermodynamic ground state, which is the spherical coacervate (**Figure 2E,** *SI Appendix* **Figure S1D**). Despite their spherical nature, these annealed assemblies spontaneously matured to a solid-like state, as evidenced by their inability to fuse or wet a glass surface (**Figure 2E-F,** *SI Appendix* **Figure S1D**).

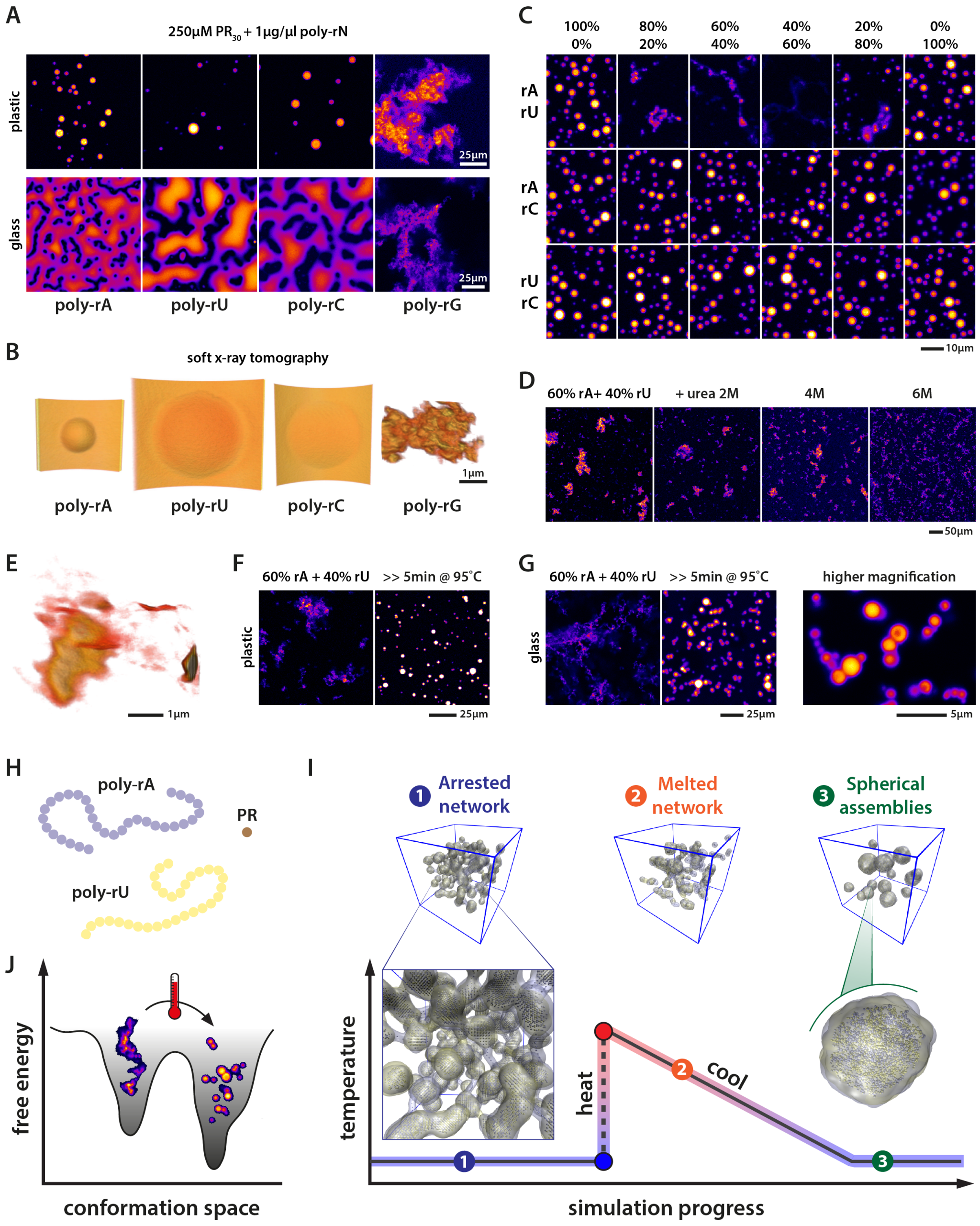

Figure 2: RNA structure determines condensate morphology. (A) All RNA homopolymers except poly-rG induce the formation of spherical liquid droplets. The liquid droplets can fuse and wet a glass surface. In contrast, poly-rG-PR complex coacervation yields distinct morphologies that are akin to large open, fractal-like networks. (B) Soft x-ray tomography images of PR-homopolymeric RNA coacervates. Poly-rA, poly-rC and poly-rU droplets wet the surface of the capillary. In contrast, poly-rG-PR systems form open three-dimensional networks. (C) Mixing homopolymeric RNA molecules that can make complementary base pairs indicates that base pairing can induce morphological transitions in PR-RNA coacervates, and this is tuned by the stoichiometry of the interacting RNAs. In contrast, morphological transitions were not observed in the presence of homopolymeric RNA molecules that cannot make complementary base pairs. (D) Urea interferes with poly-rA:rU base pairing and disrupts the formation of large networks. (E) Soft x-ray tomography of PR-poly-rA:rU (60:40) coacervates illustrates formation of aspherical granules linked by sheet-like low-density connections. (F) Boiling PR-poly-rA:rU coacervates melts A:U base pairing and results in spherical assemblies. (G) Boiled PR-poly-rA:rU coacervates fail to fuse and wet the glass surface. (H) In our minimal polymer model poly-rA and poly-rU are represented as polymers of multivalent beads while PR is a single bead, reflecting the relative differences in molecular weight and contour length. (I) Schematic showing the formation of open but arrested networks when mixtures of polymers that engage in strong intermolecular interactions (as is the case for base pairing RNAs) are simulated together. These arrested networks resolve to spherical assemblies through a heating and cooling process, as observed in simulations here and experimentally in panels F and G. PR not shown for clarity. (J) Schematic illustrating a putative energy landscape associated with complementary homopolymeric RNAs in the presence of PR. The open networks observed in panels C-G are metastable states corresponding to minima on the left, while lower energy spherical assemblies are shown on the right. Heating and cooling facilitates network re-arrangement into spherical assemblies.

Next, we asked if simulations based on phenomenological models would reproduce the findings from experiments and thereby provide a coherent explanation for our findings. To this end, we performed simulations using a coarse-grained four-component model consisting of PR, poly-rA, poly-rU and a solvent wherein long-range electrostatic interactions are effectively screened (see methods for simulation details). In these simulations, poly-rA, poly-rU, and PR form homogeneous dispersed phases in binary mixtures of these molecules with solvent. However, in simulations of ternary systems that include poly-rA, PR, and solvent or poly-rU, PR, and solvent we observed the formation of spherical condensates (*SI Appendix* **Figure S3A,B,C**). Simulations suggest that spherical condensates readily deform and the molecules within them undergo rapid-rearrangements (**Movie S4**). In contrast, in simulations of quaternary systems that include poly-rA, poly-rU, PR, and solvent, we observed the formation of open, percolated networks that are characterized by complementary poly-rA:rU interactions. While PR partitions into these networks, the resulting assemblies relax slowly, and this behavior is indicative of a kinetically trapped phase. However, upon heating, this open network melts and undergoes a re-arrangement to form spherical droplets (**Figure 2I Movie S5**). The effective mean-field energy associated with the spherical droplet phase is significantly lower than the energies associated with the open network (*SI Appendix* **Figure S4**). This provides support for the hypothesis that metastable mesophases form due to the networking of base paired RNA molecules. Additionally, simulations with a reduced poly-rA-poly-rU interaction strength directly lead to spherical assemblies, bypassing the formation of open networks (*SI Appendix* **Figure S3E**). Taken together, our computations show that higher-order RNA assemblies can provide a stable scaffold for the recruitment of a dynamic protein phase, but also that the resulting protein-RNA assemblies can exist in a metastable phase, determined by the competition between RNA base pairing and RNA-peptide interactions. These observations are concordant with physical theories that describe gelation in colloidal systems wherein the formation of open, percolated networks is viewed as kinetically arrested phase separation (53).

RNA-peptide and RNA-RNA interactions determine condensate viscosity and protein dynamics: Poly-rA, poly-rU, and poly-rC molecules can drive the formation of condensates via complex coacervation with PR molecules. The resultant condensates have similar micron-scale morphologies. Dynamical properties within condensates are governed by molecular densities, the extent of physical crosslinking, and the timescales associated with these crosslinks (54). Accordingly, we asked if condensates formed by different RNA molecules and similar proteins have intra-condensate dynamics that vary depending on the type of RNA. Condensates formed with poly-rA were more viscous than those formed by poly-rC and poly-rU as assessed by induced and spontaneous fusion of condensates (**Figure 3A-B**). Next, we investigated the set of interactions that were the main contributors to the observed differences in condensate dynamics (**Figure 3C**). The differences in viscosity associated with distinct polyribonucleotide-PR condensates may be caused by stronger polyribonucleotide-PR interactions, by stronger intrinsic interactions amongst polyribonucleotides, or by some combination of the two. To disentangle these effects, we asked if different RNA homopolymers had different intrinsic interaction strengths with themselves. We induced RNA phase separation in the absence of PR by adding a crowding agent (30% polyethylene glycol, PEG) and magnesium chloride (**Figure 3D**). Under these conditions, poly-rA, poly-rC, and poly-rU form spherical, liquid-like droplets. However, poly-rA droplets fuse more slowly when compared to poly-rU and poly-rC RNA droplets, implying a difference in intrinsic interaction strengths that define the strengths of intra-droplet interactions and the interfacial tension between the droplet and dispersed phases.

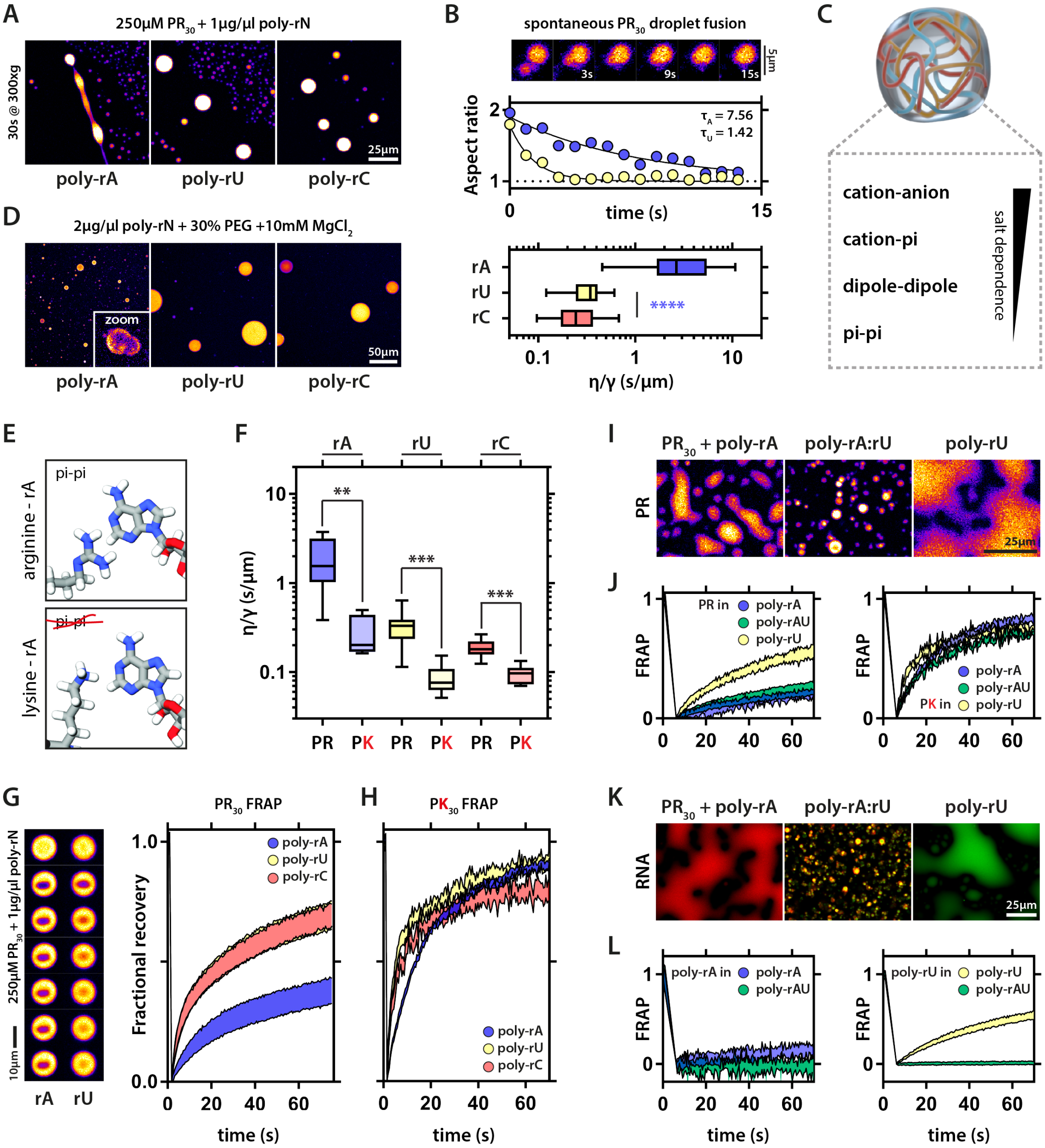

Figure 3: RNA-peptide and RNA-RNA interactions determine viscosity and protein dynamics within condensates. (A) PR-poly-rA condensates are more viscous than poly-rU and poly-rC condensates upon induced fusion via mild centrifugation. (B) PR-poly-rA condensates are more viscous as assayed by spontaneous fusion events. Relaxation curves that illustrate minimization of surface tension allow for the calculation of the (viscosity/surface tension) ratio (see materials & methods). n=10, 1-way ANOVA. Boxplots, whiskers indicate range. (C) Potential molecular interactions involved in PR-RNA coacervation. (E) Scheme indicating that arginine but not lysine can engage in pi-like interactions with the adenine base. (F) PK-polynucleotide droplets are uniformly less viscous than PR-polynucleotide droplets as assayed by spontaneous fusion events. n=8, 1-way ANOVA. Boxplots, whiskers indicate range. (G) PR is less dynamic in PR-poly-rA droplets as compared to PR in PR-poly-rU and in PR-poly-rC droplets, as assayed by FRAP. Normalized traces also show the standard deviations. (H) PK dynamics assayed using FRAP experiments are largely similar for different homopolymeric RNAs. Traces indicate SEM. (I) Examples of PR fluorescence in poly-rA and poly-rU condensates / droplets, and poly-rA:rU gels. (J) FRAP dynamics for PR and PK in poly-rA and poly-rU condensates, and poly-rA:rU gels. Traces indicate SEM. (K) Examples of poly-rA (red) and poly-rU (green) fluorescence in poly-rA and poly-rU droplets, and poly-rA:rU solid-like gels. (L) FRAP dynamics for poly-rA and poly-rU in PR-induced poly-rA and poly-rU droplets, and poly-rA:rU solid-like gels. Traces indicate SEM.

Previous work showed that PR proteins engage in specific interactions with aromatic amino acids (33). Purine-containing nucleobases (adenine and guanine) contain a double ring system while pyrimidines (cytosine and uracil) contain a single ring (*SI Appendix* **Figure S5**). Therefore, we hypothesized that in addition to the electrostatic interactions amongst PR and RNA molecules, PR may also engage in short-range, directional, so-called cation-pi interactions with the aromatic RNA bases. In proteins, tryptophan has been proposed to mediate stronger cation-pi interactions when compared to the single ring systems of phenylalanine and tyrosine (55). It is also worth emphasizing that the strength and nature of cation-pi interactions depend not only on the aromatic system, but also on the identity of the cation. The guanidinium groups of Arg sidechains are Y-shaped planar moieties that are best described as cross-conjugated pi systems implying that six pi electrons are likely to be delocalized across the functional group. From a classical perspective, moieties with pi-like structures will have high intrinsic quadrupole moments (56). Sidechains such as Tyr and Trp will be endowed with high intrinsic dipole moments whereas Arg will have monopole, dipole, and quadrupole moments. In contrast, the tertiary amine of Lys, which is a cation, will have a monopole moment that is identical to that of Arg, but its dipole and quadrupole moments are negligible (56). These features enable a hierarchy of protein-protein and protein-RNA interactions (57, 58). Specifically, it has been shown that arginine drives stronger interactions with tyrosine and phenylalanine than lysine (40, 55, 57, 58). These findings, in conjunction with our initial observations regarding the intrinsic interactions amongst poly-rA molecules lead to two testable hypotheses. First, we propose that PR should interact more strongly with poly-rA than with either poly-rU or poly-rC. Second, RNA should interact more strongly with PR than an equivalent length proline-lysine (PK) dipeptide repeat. We used bio-layer interferometry to quantify the apparent strengths of PR interactions with different RNA molecules. Our data suggest that the PR-poly-rA interaction is the strongest, while PR-poly-rU and PR-poly-rC interactions are almost identical to one another (*SI Appendix* **Figure S2**). Interestingly, the apparent dissociation constant (K_d) was highest (lowest apparent affinity) for poly-rG. We interpret these results to mean that the effects of rG-rich RNA sequences on the PR phase behavior derives from the inability of PR to outcompete base stacking interactions associated with G-quadruplex formation.

Next, we compared the phase behaviors of PR with a $(PK)_{30}$ peptide (PK). Lysine has a similar positive charge as arginine, and also engages in cation-pi interactions. However, it lacks the apparent Y-aromaticity of the guanidinium group and cannot encode the hierarchy of interactions attributable to the higher-order multipole moments of Arg (57) (**Figure 3E**). We find that condensates formed using the PK peptide displayed reduced viscosity irrespective of the RNA sequence. Interestingly, we observe the largest decrease in viscosity for PK-poly-rA droplets, implying a reduction in the strength of interaction between PK and RNA compared to PR (**Figure 3F**). These findings suggest that networks of interactions among arginine residues and the nucleobases are involved in tuning droplet dynamics. When we examined PR dynamics, rather than droplet dynamics, we obtained similar results (**Figure 3G**). PR was less dynamic in poly-rA droplets compared to the others, in agreement with inferences based on bio-layer interferometry (*SI Appendix* **Figure S2**). As for dynamics, PK was more dynamic than PR and the differences between the RNAs were largely reduced (**Figure 3H**). Taken together, these findings illustrate that hierarchies of molecular interactions amongst the protein and RNA components influence both nano- (intra-droplet diffusion) and micron-scale dynamics (droplet fusion). These results are analogous to the recent findings of Wang et al. (57) who showed that a hierarchy of interactions combined with a so-called stickers and spacers model explains their data for the phase behavior of FUS family proteins.

RNA concentration determines protein dynamics: Previous studies showed that PR undergoes phase separation in the absence of RNA providing a suitable macromolecular crowder was added (33). Under these conditions the positive charges of the arginine residues appear to be neutralized by anions present in the buffer (e.g., phosphate groups). By driving PR-only droplet formation with PEG as a molecular crowding agent, additional

RNA (poly-rU) molecules should partition preferentially into the condensate by enabling the release of neutralizing mobile anions. This could provide a route to increase the intra-droplet concentration of RNA. As can be seen in *SI Appendix* **Figure S6**, PR-only droplets display reduced dynamics when compared to RNA-only droplets (**Figure 3G**) due to the higher viscosity of the solution (i.e., 30 wt% PEG). However, the stepwise increase in RNA concentration further reduces the FRAP recovery and dynamics of PR in the droplets (*SI Appendix* **Figure S6**). Indeed, the half-life for FRAP correlates with the total concentration of added RNA. This observation indicates that the number density of interaction sites provided by protein and RNA can determine coacervate dynamics in a similar way to the interaction strength.

RNA gelation induces coexistence of material states: In assemblies formed from complementary RNAs and PR, RNA base pairing can induce the formation of solid-like gels that can be either metastable open networks or globally stable spherical solid-like assemblies (**Figure 2F**). Accordingly, we asked if the dynamics of either PR or PK would be influenced by the material states of RNA. To investigate this, we first examined the dynamics of PK and PR in solid-like spherical assemblies formed by base pairing RNA (poly-rA:rU) after heating and those in liquid-like droplets with poly-rA or poly-rU. Surprisingly, we found that the dynamics of the peptides were completely independent of RNA dynamics (**Figure 3I-J**). In addition, PK was significantly more labile in poly-rA and poly-rA:rU droplets than PR. These results illustrate that an assembly with apparent solid-phase behavior, as gleaned from the dynamics of RNA molecules, can still support a fluid phase. This points to the coexistence of liquid-like properties for the proteins and solid-like properties for the complementary RNA molecules akin to a hydrogel (a solid polymeric scaffold supporting a second internal liquid phase).

Having examined protein dynamics within protein-RNA coacervates, we next examined the dynamics associated with distinct types of RNAs in different condensates. Firstly, poly-rA molecules are less labile than poly-rU molecules in their respective condensates (**Figure 3K-L**). This result is in agreement with the finding that for both pure RNA condensates and PR/PK-RNA condensates, those containing poly-rA are always more viscous than those containing poly-rU (**Figure 2D-F**). Secondly, in the poly-rA:rU RNA gels both RNAs were completely immobile. This is in stark contrast to the PR and PK peptides, which remain fully labile. This finding, in agreement with results in **Figure 1**, demonstrates that multicomponent condensates can support overlapping spatial distributions and distinct, decoupled dynamics of the molecular components. Therefore, even in unitary condensates, i.e., condensates where the protein and RNA molecules are apparently well mixed, the dynamical behaviors of protein and RNA molecules can be different from one another. This is achieved purely through the nature of the underlying molecular interactions and does not require active processes. The behavior we observe for differential dynamics within an apparently well-mixed condensate is reminiscent of the postulates of viscoelastic phase separation, which is governed by the differential mobilities of constituent molecules (59) .

Mixing RNA species generates complex multi-layered condensates: We have shown that RNA concentration, sequence, and structure can alter the driving forces for phase separation and the dynamics of the resultant condensates. Mixing non-base pairing RNAs does not alter condensate formation. However, when we induce the fusion of these condensates to enable the formation of larger scale droplets through gentle centrifugation, we observe the formation of multi-layered topologies (**Figure 4A-B**). Interestingly, we also observed different topologies when varying the stoichiometry of poly-rA and poly-rC. On both ends of the stoichiometry spectrum we have uniform condensates (as observed by PR fluorescence), yet gradually they evolve to a core/shell topology observed around a 50:50 mix of the RNAs (**Figure 4A**). Using soft x-ray tomography, which has a higher spatial resolution than standard confocal microscopy, we observe multi-layered topologies in condensates that have more representative dimensions of cellular membraneless organelles (**Figure 4C-D, Movie S6**). Therefore, multi-layered assemblies can arise due to spontaneous fusion and Ostwald ripening events, and are not an artifact of centrifugation. Importantly, we identify sub-compartments based on differences in x-ray absorbance, suggesting that the multi-layered architectures have defined and observable differences in molecular density.

Multi-layered condensates support differential partitioning of biomolecules: Our initial observation was that depending on the RNA stoichiometry certain compartments had a higher PR intensity. Given that PR has a stronger binding affinity for poly-rA than poly-rC (*SI Appendix* **Figure S2**), and a higher partitioning ratio for poly-rA than poly-rC droplets (**Figure 4E**), we reasoned that in the 50:50 stoichiometry, we were observing a poly-rA droplet (core) surrounded by a poly-rC shell. We subsequently tested the effects of low complexity domains derived from two well-studied RNA-binding proteins and RNAs for similar preferential partitioning into one compartment over another. These experiments allowed for tests of how RNA might encode differential partitioning in multi-layered topologies. The FUS and hnRNPA2 low complexity domains (LCD) are sufficient to undergo phase separation independently (39, 60), and showed modest partitioning into PR-RNA droplets. We observed that the hnRNPA2 LCD did not have a preference for poly-rA over poly-rC condensates, whereas for the FUS LCD we observed a clear preference for poly-rA over poly-rC (**Figure 4E**). Accordingly, we predicted that in a multi-layered condensate comprising of poly-rA and poly-rC, the hnRNPA2 LCD would not show differential partitioning, while FUS LCD should display a preference for the poly-rA core. As can be seen in **Figure 4E**, this was indeed the case. These preferences are interpretable in terms of sequence-encoded interactions of LCDs. The LCD of FUS lacks charged residues, but it contains a large number of tyrosine residues. These tyrosine residues appear to drive preferential interactions with poly-rA via a hierarchy of interactions. This proposal is consistent with results indicating that poly-rA is able to engage in stronger interactions due to its double-ringed nucleobase (*SI Appendix* **Figure S7**). In contrast the hnRNPA2 LCD contains fewer tyrosine residues and also includes cationic arginine residues. These features appear to engender equivalent interactions for both poly-rA and poly-rC (*SI Appendix* **Figure S7**).

We made similar observations for short RNA probes. While oligo-rA and oligo-rU preferred condensates formed by poly-rA as opposed to poly-rC, oligo-rC showed a preference for the condensates formed by poly-rC (**Figure 4F**). Hence, multi-layered poly-rA-poly-rC condensates are predicted to enrich poly-rA and poly-rU in the core versus poly-rC in the shell. These predicted preferences from the single condensate observations were congruent with observations in the multi-layered condensate system (**Figure 4F**). In contrast, rather than a preference for poly-rC, we propose that poly-rC oligomers are unable to outcompete stronger poly-rA-poly-rA interactions and are preferentially excluded from poly-rA condensates. This gives rise to an effective preferential partitioning into poly-rC condensates where this competition is no longer relevant. These findings indicate that partitioning in complex topological settings might follow predictable trends for the respective phases in simpler single-phase condensates – an observation that is reminiscent of the findings from the work of Feric et al. (19).

Since poly-rA and poly-rC layers seem to preserve their affinity for certain biomolecules we also asked if the characteristic dynamics of these layers would be retained in multilayered condensates. Upon interrogation of the differences in layer-specific dynamics within multi-layered condensates we observed similar relative differences that are in accord with predictions from the single-phase condensates (i.e., poly-rA is less labile than poly-rC), irrespective of the relative topology (**Figure 4G-H**). This indicates that single compartment behaviors are predictive of the compartmental dynamics associated with more complex condensate topologies.

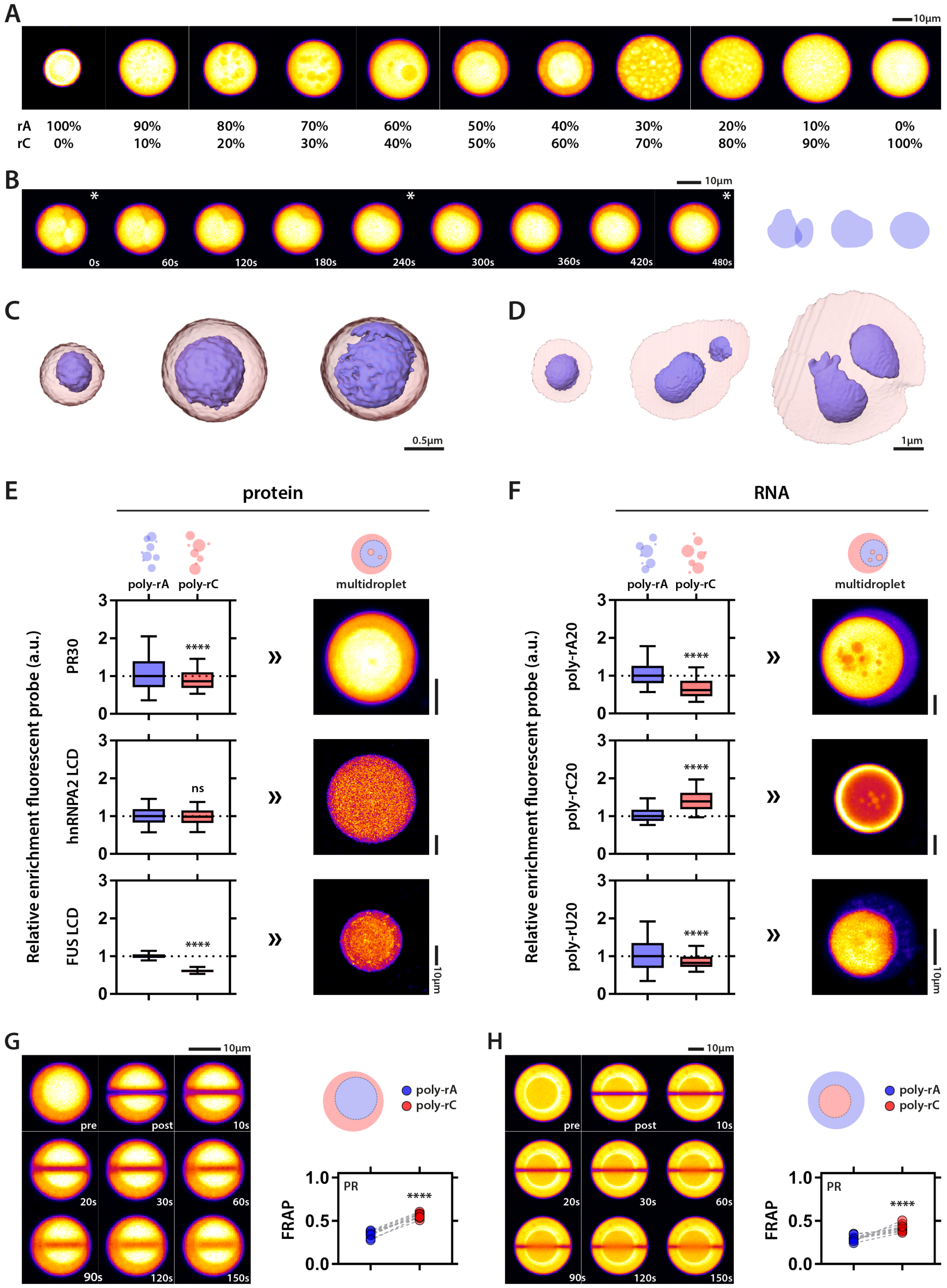

Figure 4: PR molecules combined with RNA mixtures generate multi-layered condensates with differential partitioning of biomolecules. (A) Condensates show PR fluorescence. Mixing poly-rA and poly-rC results in sub-compartmentalization, as seen via differences in PR intensity. The sub-compartmentalization is tuned by the stoichiometry of poly-rA to poly-rC. Exposure settings are different between condensates to enhance visibility of sub-compartments. (B) Internal droplets behave as liquids as probed by their fusion dynamics. Stars indicate frames corresponding to scheme on the right. Data are shown for 50:50 ratio of poly-rA-poly-rC. (C-D) Three-dimensional models of multi-layered condensates (50:50) as imaged by soft x-ray tomography. (C) Free multi-layered condensates. (D) Multi-layered condensates that wet the capillary surface. (E) Differential protein partitioning in multi-layered condensates is predicted by partitioning in single RNA droplets. Fluorescence of the indicated probe molecule is shown. (F) Differential partitioning of RNA also follows partitioning preference of single RNA condensates. (E-F) Multi-layered condensates are generated by 50:50 poly-rA-poly-rC mixtures. Boxplots, whiskers indicate range. Statistical analysis was performed using the Student t-test. (G) Internal poly-rA droplets are less dynamic than their corresponding poly-rC shells. 50:50 poly-rA-poly-rC (H) Internal poly-rC droplets are more dynamic than their corresponding poly-rA shells. 60:40 poly-rA-poly-rC. (G-H) Paired values for poly-rA and poly-rC compartment are shown for each multi-droplet. Statistical analysis was performed using the Student t-test.

Equivalent multi-layered topologies can be achieved through multiple independent mechanisms: Given the observed multi-layered topologies and the range of distinct interactions, we next asked if we could unambiguously determine the molecular origins of the multi-layered topologies. Specifically, given a ternary mixture of PR, poly-rA, poly-rC and solvent, what types of interactions could give rise to the observed core/shell architecture? To answer this question, we again turned to coarse-grained simulations (see methods for additional details). Equivalent core/shell topologies could be achieved through a number of entirely independent interaction mechanisms. For example, if poly-rA preferentially binds PR over poly-rC, then a dense PR-poly-rA core forms and a PR-poly-rC shell surrounds the core. The formation of this topology depends both on the relative mismatch in PR binding and on the absolute concentration of free PR. If poly-rA-PR binding is too strong and there is insufficient PR, then poly-rA will effectively sequester the majority of the PR, preventing poly-rC from coalescing or only allowing a thin shell of poly-rC to form over the poly-rA condensate periphery (*SI Appendix* **Figure S8A-B**). An alternative route to the observed core-shell topology is realized if poly-rA interacts with itself more strongly than poly-rC. Importantly, for this to give rise to a single multi-layered condensate, poly-rA-poly-rC interactions must be more favorable than poly-rC-poly-rC interactions. If this is not the case, then two distinct droplets will form (*SI Appendix* **Figure S8C**). Finally, if poly-rA experiences less favorable interactions with the solvent when compared to poly-rC, then a poly-rA core will form to reduce the solvent-poly-rA interactions while an enveloping poly-rC shell will engulf the core. Examples of these three distinct scenarios are shown in **Figure 5**, along with the associated interaction tables that give rise to the resulting topologies. In each of the three cases, a single set of interactions is modulated while the others remain fixed. Our simulation results suggest that the spatial organization of condensates can be tuned in distinct, synergistic, and antagonistic ways, thus providing routes for condensate assembly and disassembly.

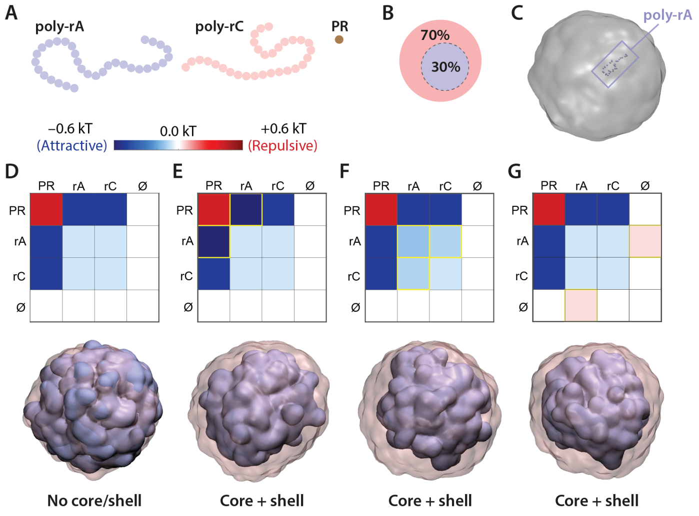

Figure 5: Core-shell multi-layered condensates can be formed via several distinct mechanisms. (A) Schematic of the molecular entities included in simulations based on the coarse-grained model that includes poly-rA, poly-rC and PR. (B-C) Simulations are run with 70:30 split of poly-rC-poly-rA and give rise to droplets that are significantly larger than individual polymers. (D-G) A suitable interaction table defines the attractive and repulsive interactions between individual beads. These effective pairwise interactions represent the cumulative interplay among all bead-bead and bead-solvent interactions. Yellow boxes highlight differential values compared to panel D. When poly-rA and poly-rC are equivalent to one another a single well-mixed droplet is formed (D). If poly-rA-PR interaction is stronger than poly-rC-PR interaction (E), if poly-rA-poly-rA interaction is stronger than poly-rC-poly-rA interaction which us in turn is stronger than poly-rC-poly-rC interaction (F), or if poly-rA-solvent is more repulsive than poly-rC-solvent, then topologically equivalent multi-layered condensates are formed. Experimental data suggest that all three mechanisms may occur, to varying degrees.

DISCUSSION

Biomolecular condensates harbor a complex mixture of hundreds of different RNA and protein species *in vivo* (17, 26, 27, 61, 62). This makes it challenging to uncover specific molecular functions and / or quantify interactions of specific RNA or protein molecules within condensates. These molecular functions are likely to be important for mesoscale functions of condensates. Here, we resorted to a simple test tube model of RNA protein granules, based on biologically relevant PR proteins, which allows us to dissect the underlying physico-chemical forces that drive specific behaviors. We show that biological polyanions drive phase separation of Arg-rich proteins through complex coacervation, albeit with significant chemical specificity. The morphologies and material states of the resulting phases vary dramatically with polyanion type. To understand the role of RNA sequence and structure we focused on simple homopolymeric RNA molecules. We found that stable RNA secondary structure formation leads to rigid open networks. In contrast, RNA molecules lacking stable secondary structure promote the formation of liquid-like condensates. Based on denaturing-annealing reactions and computer simulations, we show that the open networks represent metastable phases that arise from barriers governed by a competition between RNA base pairing and RNA-protein interactions. When released from their metastable phases the resulting molecular rearrangements lead to an annealing toward spherical condensates. However, solid-like behavior of RNA molecules can persist within spherical condensates and we propose, based on extant data, that this derives from the formation of condensate spanning networks via physical crosslinks (i.e., gelation) that determine rheological properties. Despite the immobility of RNA within the assemblies, the condensates support a protein phase that exhibits rapid dynamics that are indistinguishable when compared to liquid droplets. Our findings indicate that RNA base pairing can decouple RNA and protein dynamics and lead to a coexistence of different molecular level dynamics within the same condensate. This observation has major implications for the description of cellular condensates: *Rapid dynamics of one* (*protein or RNA*) *component does not necessarily mean the condensate as a whole behaves as a liquid*.

Besides RNA base pairing, RNA sequence and the purine / pyrimidine contents are also key regulators of the material properties of condensed phases. Nano- and micron-scale dynamics of protein-RNA condensates are tuned by the interplay amongst RNA-RNA, RNA-protein, RNA-solvent, and protein-solvent interactions. We showed that by mixing different homopolymeric RNAs we can induce spontaneous sub-compartmentalization within condensates, and that this can be tuned by varying RNA stoichiometries. These multi-layered condensates enable differential partitioning of other biomolecules while also displaying differential protein dynamics. These findings provide a touchstone for understanding the *in vivo* phase behavior of heterogeneous mixtures of protein and RNA molecules. Our coarse-grained simulations indicate that core-shell architecture arise from the differential effects RNA-protein, RNA-RNA, RNA-solvent, and protein-solvent interactions.

Multi-layered condensates have previously been reported for mixtures of nucleolar protein and RNA molecules (19) and synthetic multivalent proteins (21, 63). As was shown previously for nucleolar proteins (19), we also found that differential surface tension determines the preferential partitioning of molecules into the cores versus shells in multi-layered condensates. These findings are borne out in coarse-grained simulations. However, simulations do not show the formation of multi-layered condensates in which the denser poly-rA phase exists as a shell around a less-dense poly-rC core, as observed in **Figure 4A** and **4H**. The formation of this ‘inverted’ topology would be at odds with a simple equilibrium thermodynamic model. Yet, for multi-layered condensates in which the difference in surface tension between distinct phases is low and those phases are relatively viscous, these inverted topologies could form in response to some initial mixing or other energy input. Moreover, once formed, there may be a large energetic barrier associated with topological re-organization. Since we did not observe these apparently metastable states in smaller multi-layered condensates (as imaged with SXT), but did find them in larger multi-layered condensates formed via mild centrifugation, it is possible that the inverted multi-layered condensates derive from the energy that is supplied during the centrifugation process. It is worth noting that similar inverted topologies have been observed for condensates in cells. Overexpression of a TDP-43-derived fusion protein results in the formation of large nuclear droplets that contain “vacuoles” of nucleoplasm (64). Vacuolization has also been observed when nucleoli fuse together due to destabilization of the nuclear actin cytoskeleton (19). This suggests that fusion events, especially of larger more viscous droplets, may provide enough energy to drive multi-layered condensates into metastable states, both in the test tube and in cells.

Our findings combined with recent studies of Maharana et al. (65) and Langdon et al. (66) show that RNA structure, RNA-to-protein ratios, and the interplay of RNA-RNA, protein-protein, and protein-RNA interactions contribute to the complex topologies of protein-RNA condensates as well as their material properties. It appears that many of the features observed *in vivo* for protein-RNA condensates can be recapitulated *in vitro* and that these features are the result of spontaneous (passive), sequence-encoded driving forces rather than driven (active) processes. The rules we have gleaned further refine the questions we get to ask about the interplay between spontaneous (passive) versus driven (active) processes *in vivo*. A proposal that emerges from our work is that active processes mainly modulate or maintain the sequence-encoded properties of condensates that form via spontaneous thermodynamic control. Our results also highlight key design challenges and opportunities that could inspire new nanomaterials and drug delivery strategies. This is relevant given the rising popularity of nucleic acid-based nanotechnology (67-70) and therapy (71, 72), including arginine-rich peptide-nucleic acid coacervates (73-76),

MATERIAL AND METHODS

Polyanions, synthetic peptides and recombinant proteins

Poly-rU, poly-rC, poly-rG, poly-rA, total yeast RNA, heparin, chondroitin and polyphosphate were purchased from Sigma-Aldrich. Albumin was purchased from Rockland, Inc. Microtubules were purchased from Cytoskeleton Inc. rRNA was purchased from Bio-World. Salmon sperm DNA (ssDNA) was purchased from Ambion (Thermo Scientific). All polyanions were dissolved in milli-Q water and stored at −20°C. We purchased chemically synthesized peptides from Pepscan (Lelystad, Netherlands). Peptides were dissolved in milli-Q water and stored at −20°C. FUS and hnRNPA2 LC domains were expressed in E. coli and purified as described previously (39, 60). Peptides and proteins were fluorescently labeled using Alexa Fluor Labeling Kits (Thermo Scientific). Fluorescent RNA oligomers were synthesized by IDT. Fluorescent peptides or RNA oligomers were spiked in at 200 nM and 100 nM respectively as final concentrations. Fluorescent low complexity domains (LCDs) were spiked in at 1 µM.

Induction of phase separation

Polyanions were diluted to 1 µg/µL in 100 mM K_2HPO_4 / KH_2PO_4 buffer at pH 7. Peptides were added at 250 µM concentrations. All reactions were carried out at room temperature (≈ 25˚C), unless indicated otherwise. For fluorescence microscopy and FRAP analyses, labeled peptides were spiked in at 1 µM. For partitioning experiments, probe molecules were spiked in at 100 nM. For the generation of pure RNA liquid droplets, homopolymeric RNAs were diluted to 2 µg/µL in 1x PBS buffer with 30% PEG and 10 mM $MgCl_2$ at pH 7.

Bio-layer interferometry (BLI)

Homopolymeric RNAs (Sigma) were N-terminally biotinylated (ThermoFisher, 20160) and immobilized on super streptavidin biosensors (ForteBio, 18-5065) in Octet RED96 device (FortBio), at 70 µg/mL concentration for 80s at RT. The following average response values were reached at the sensor loading step, poly-rU: 0.20 ± 0.02 nm, poly-rA: 0.22 +/- 0.03 nm, poly-rC: 0.19 ± 0.03 nm, poly-rG: 0.23 ± 0.01 nm. Sensors were subsequently blocked in 0.01mg/ml biocytine for 60s and washed. After recording baseline in fresh buffer, association was performed in increasing concentration of PR30 (0 nM, 10 nM, 100 nM, 250 nM, 600 nM, 1 µM) for 400 s and dissociation was followed in the same well where baseline was recorded for 800s. Interferograms were background corrected with traces recorded on biocytine blocked sensors, immersed into the same PR30 samples. Every component throughout the experiment was dissolved in 1x kinetic buffer (ForteBio), supplemented with PBS, according to the manufacturer's guidelines. Individual concentration curves were fitted with a ForteBio analysis software, using 1:1 kinetics model, and values extracted for individual experiments. Saturation values of association phase were then transferred to GraphPad Prism 7.02, plotted in the function of PR30 concentrations.

Fluorescence recovery after photobleaching (FRAP) analysis

Details of the protocol were as previously published (77). In brief, fluorescent droplets were incubated in plastic Cell Counter slides (Bio-Rad) at room temperature. Chambers were sealed using nail varnish to prevent evaporation during aging. To generate large droplets and / or large multi-layered condensates, samples were briefly centrifuged for 30 s at 1200 rpm in a bench top centrifuge 5810R (Eppendorf). Fluorescence recovery after bleaching was monitored using Zen software on a Zeiss LSM 780 Meta NLO confocal microscope equipped with a 20x long-range objective. For intra-droplet FRAP, a circular are of 1 µM radius was bleached in droplets with a radius between 5 µM and 10 µM. Raw data were background subtracted and normalized using Excel, and plotted using Graphpad Prism software. FRAP curves were fitted with a one phase exponential curve. Images were formatted using FIJI and ImageJ software.

Droplet fusion experiments

Samples with fluorescent droplets were incubated in plastic Cell Counter slides (Bio-Rad) at room temperature and immediately imaged on a Zeiss LSM 780 Meta NLO confocal microscope equipped with a 20x long-range objective. Time-lapse images were taken of droplets settling on the cover slip and fusing together. Fusion events were manually identified and measured using FIJI and ImageJ software. Relaxation curves were plotted using Graphpad Prism software and fitted with one-phase exponential decay curves. Relaxation times (τ) were calculated by Graphpad prism and used for estimating the inverse capillary velocity (η/γ) via following formula: $\tau \approx (\eta/\gamma)L$ where L is the characteristic length scale of the droplet, as described in (6, 78).

Partitioning analysis

Fluorescent droplets were incubated in plastic Cell Counter slides (Bio-Rad) at room temperature. Chambers were sealed using nail varnish to prevent evaporation during aging. Random fields of view were obtained on a Zeiss LSM 780 Meta NLO confocal microscope equipped with a 20x long-range objective. Ratio of fluorescence intensity in the droplets over the surrounding background was calculated for individual droplets using Excel, and plotted using Graphpad Prism software.

Statistical analysis

All statistical and regression analyses were carried out using Graphpad Prism. Details are indicated in the figure legends. * p-value: 0.01-0.05, ** p-value: 0.01-0.001, *** p-value: 0.001-0.0001, **** p-value < 0.0001.

Soft x-ray tomography (SXT)

After induction of phase separation, the droplets were loaded in thin-wall glass capillaries and rapidly frozen in liquid propane, for details see previous work (79, 80). The specimens were imaged by XM-2, a soft x-ray microscope in the National Center for X-ray tomography (hhttp://ncxt.lbl.gov) located at the Advanced Light Source of Lawrence Berkeley National Laboratory. The x-ray microscope operates at the “water-window” region of soft x-rays, providing natural contrast of biomolecules with respect to water. The condenser, objective lens and magnification, chosen for this experiment, guaranteed isotropic 32 nm voxel size. For 3D reconstructions, 92 projection images, with 200 ms exposure time each, were acquired sequentially around a rotation axis with 2° increment angles. After normalization and alignment, tomographic reconstructions were calculated using iterative reconstruction methods. The segmentation and visualization of multi-layered condensates was performed using linear attenuation coefficient of x-rays (81) in Amira 6.3.0.

Coarse-grained simulations

All simulations were performed using coarse-grained lattice-based models. The simulations themselves deploy Monte Carlo sampling and the brand of models deployed here has been used previously to study phase behavior (5, 20, 82). The model is based on a standard granular lattice mode in which each bead occupies a single site on the lattice, which defines the excluded volume per bead. Any given bead interacts with every adjacent lattice site and engages via bead-bead and bead-solvent interactions, where empty lattice sites are taken to be occupied by solvent. Each simulation involves more than 10^9 independent moves. Finite size artifacts were overcome by including at least 2×10^4 particles. The cubic lattices have dimensions of 80^3 or 100^3 depending on the simulation in question. Five independent simulations where run, for each simulation type, and we find extremely good agreement across independent simulation runs (*SI Appendix* **Figure S3**). Two different types of simulations were run: One set examined the formation of arrested network assemblies (**Figure 2**), and the second set examined equilibrium droplet topology associated with multicomponent droplets (**Figure 5**).

For simulations used to examine the formation of arrested network assemblies, we followed the formalism of Dynamic Monte Carlo (DMC) (83-86). In DMC, two classes of moves are performed, moves that locally perturb each bead or particle according to some limited distance that corresponds to the distance moved by the particle over some characteristic time-step, and rigid body moves that rotate or translate individual or clusters of molecules according to their molecular mass. In our implementation, we only perform the first set of moves. This leads to a slowdown in the absolute convergence times; however, the simulations are fast enough that this is of minimal practical impact. However, it also avoids the potentially misleading impact of translating species of vastly different sizes in a manner that considers only mass and not the effective hydrodynamic drag. This becomes important because $(PR)_{30}$ and polynucleotides are of dramatically different molecular weights and contour lengths (see below). Importantly, assuming we are comparing two simulations with an identical distribution of species, we are able to formally assess relative changes in relaxation and equilibration.

For the simulations performed to examine multi-layered topologies, we focused on equilibrium properties. With this in mind, in addition to the local moveset described above, we allow an additional set of Monte Carlo moves (translation, rotation, cluster translation and rotation, chain pivot) which improves sampling. In all cases, our movesets preserve detailed balance. We define arrested network assemblies as those in which the simulation reaches a state that is exponentially stable, yet demonstrably higher in energy than another configuration that can be reached via heating and cooling (simulated annealing) (*SI Appendix* **Figure S3**). In all systems, $(PR)_{30}$ and polyN (poly-rA, poly-rC, or poly-rU) are represented explicitly. The ratio of contour lengths between $(PR)_{30}$ (~300 Å) and polyN of around 600 kDa RNA (~10 000 Å) is around 1:30. Consequently, we represent each $(PR)_{30}$ molecule as a single multivalent bead, while each RNA molecule consists of 30 beads. Relative contour lengths for RNA and protein are based on a nucleotide/amino acid contour length of 5 Å and 3.6 Å, respectively. While these are clearly order-of-magnitude simplifications, varying length distributions (within the associated order of magnitude) had no material effect on results (**Figure S9**). The simulations performed represent a minimal coarse-grained model that is able to recapitulate the observed behavior. There is nothing in the model that reflects the fact that the polymers are RNA and protein, as opposed to generic polymers with specific preferential interactions. It is almost inconceivable that for naturally occurring RNA there will not be significant additional complexity associated with protein-RNA interactions. Moreover, we make no attempt to consider the impact of solution conditions. However, for a simple homopolymeric system we seem able to capture many of the macroscopically observable features with simple intuitive models. Simulation trajectories were analyzed using locally written code using filesystem operations implemented in MDTraj (87), while simulation snapshots were generated using VMD (88).

ACKNOWLEDGMENTS

The authors thank Dr. Broder Schmidt, Dr. Frederic Rousseau, Dr. Joost Schymkowitz, Dr. Sean Friedowitz, Dr. Jian Qin, Dr. Jeong-Mo Choi, and Dr. Andrea Soranno for helpful discussions. The authors also thank Dr. Nicholas L. Fawzi for his kind gift of the FUS LCD and hnRNPA2 LCD recombinant proteins, and Dr. Andrew Olson for his help with the microscopy. L.V.D.B is supported by KU Leuven ('Opening the future' and C1), the Fund for Scientific Research Flanders (FWO-Vlaanderen), the 'Agency for Innovation by Science and Technology in Flanders' (IWT-Vlaanderen) and the ALS Liga (Belgium). S.B. acknowledges a long-term fellowship from EMBO. P.T. is supported by Odysseus grant G.0029.12 from FWO-Vlaanderen. V.W. is supported by German Research Foundation research fellowship WE 6221/1-1. C.L. is supported by NIH-NIDA U01 DA040582. The National Center for X-ray Tomography is supported by NIH (P41GM103445) and DOE's Office of Biological and Environmental Research (DE-AC02-5CH11231). The contributions of A.S.H and R.V.P were supported by grants from the Human Frontier Science Program (RGP0034/2017), the US National Science Foundation (MCB-1614766), and the St. Jude Children's Research Hospital sponsored collaborative on membraneless organelles.

REFERENCES

1. Brangwynne CP, Tompa P, & Pappu RV (2015) Polymer physics of intracellular phase transitions. *Nat Phys* 11(11):899-904.
2. Hyman AA, Weber CA, & Julicher F (2014) Liquid-liquid phase separation in biology. *Annu Rev Cell Dev Biol* 30:39-58.
3. Boeynaems S*, et al.* (2018) Protein Phase Separation: A New Phase in Cell Biology. *Trends Cell Biol*.
4. Shin Y & Brangwynne CP (2017) Liquid phase condensation in cell physiology and disease. *Science* 357(6357).
5. Harmon TS, Holehouse AS, Rosen MK, & Pappu RV (2017) Intrinsically disordered linkers determine the interplay between phase separation and gelation in multivalent proteins. *eLife* 6.
6. Brangwynne CP*, et al.* (2009) Germline P granules are liquid droplets that localize by controlled dissolution/condensation. *Science* 324(5935):1729-1732.
7. Banani SF, Lee HO, Hyman AA, & Rosen MK (2017) Biomolecular condensates: organizers of cellular biochemistry. *Nat Rev Mol Cell Biol* 18(5):285-298.
8. Berry J, Brangwynne CP, & Haataja M (2018) Physical principles of intracellular organization via active and passive phase transitions. *Reports on Progress in Physics* 81(4):046601.
9. Kedersha N, Ivanov P, & Anderson P (2013) Stress granules and cell signaling: more than just a passing phase? *Trends Biochem Sci* 38(10):494-506.
10. Protter DS & Parker R (2016) Principles and Properties of Stress Granules. *Trends Cell Biol* 26(9):668-679.
11. Anderson P, Kedersha N, & Ivanov P (2015) Stress granules, P-bodies and cancer. *Biochim Biophys Acta* 1849(7):861-870.
12. Boeynaems S, Bogaert E, Van Damme P, & Van Den Bosch L (2016) Inside out: the role of nucleocytoplasmic transport in ALS and FTLD. *Acta Neuropathol*.
13. Li YR, King OD, Shorter J, & Gitler AD (2013) Stress granules as crucibles of ALS pathogenesis. *J Cell Biol* 201(3):361-372.
14. Ramaswami M, Taylor JP, & Parker R (2013) Altered Ribostasis: RNA-Protein Granules in Degenerative Disorders. *Cell* 154(4):727-736.
15. Boeynaems S, Tompa P, & Van Den Bosch L (2018) Phasing in on the cell cycle. *Cell Division* 13(1):1.
16. White JP & Lloyd RE (2012) Regulation of stress granules in virus systems. *Trends Microbiol* 20(4):175-183.
17. Jain S*, et al.* (2016) ATPase-Modulated Stress Granules Contain a Diverse Proteome and Substructure. *Cell* 164(3):487-498.
18. Wheeler JR, Matheny T, Jain S, Abrisch R, & Parker R (2016) Distinct stages in stress granule assembly and disassembly. *Elife* 5.
19. Feric M*, et al.* (2016) Coexisting Liquid Phases Underlie Nucleolar Subcompartments. *Cell* 165(7):1686-1697.
20. Fei JY*, et al.* (2017) Quantitative analysis of multilayer organization of proteins and RNA in nuclear speckles at super resolution. *J Cell Sci* 130(24):4180-4192.
21. Harmon TS, Holehouse A, S. , & Pappu R, V. (2018) Differential solvation of intrinsically disordered linkers drives the formation of spatially organized droplets in ternary systems of linear multivalent proteins. *New Journal of Physics* 20(4):045002.
22. Holehouse AS & Pappu RV (2018) Functional Implications of Intracellular Phase Transitions. *Biochemistry* 57(17):2415-2423.
23. Boulon S, Westman BJ, Hutten S, Boisvert FM, & Lamond AI (2010) The nucleolus under stress. *Mol Cell* 40(2):216-227.
24. Jin M*, et al.* (2017) Glycolytic Enzymes Coalesce in G Bodies under Hypoxic Stress. *Cell reports* 20(4):895-908.
25. Srivathsan Adivarahan SR, Daniel Zenklusen (2017) Spatial organization of single mRNPs at different stages of the gene expression pathway. *BioRxiv*.

26. Khong A*, et al.* (2017) The Stress Granule Transcriptome Reveals Principles of mRNA Accumulation in Stress Granules. *Mol Cell* 68(4):808-820 e805.
27. Namkoong S, Ho A, Woo YM, Kwak H, & Lee JH (2018) Systematic Characterization of Stress-Induced RNA Granulation. *Mol Cell*.
28. Van Treeck B*, et al.* (2018) RNA self-assembly contributes to stress granule formation and defining the stress granule transcriptome. *Proc Natl Acad Sci U S A* 115(11):2734-2739.
29. Jain A & Vale RD (2017) RNA phase transitions in repeat expansion disorders. *Nature* 546(7657):243-247.
30. Zhang H*, et al.* (2015) RNA Controls PolyQ Protein Phase Transitions. *Mol Cell* 60(2):220-230.
31. Berry J, Weber SC, Vaidya N, Haataja M, & Brangwynne CP (2015) RNA transcription modulates phase transition-driven nuclear body assembly. *Proc Natl Acad Sci U S A* 112(38):E5237-5245.
32. Caudron-Herger M*, et al.* (2015) Alu element-containing RNAs maintain nucleolar structure and function. *EMBO J* 34(22):2758-2774.
33. Boeynaems S*, et al.* (2017) Phase Separation of C9orf72 Dipeptide Repeats Perturbs Stress Granule Dynamics. *Mol Cell* 65(6):1044-1055 e1045.
34. Lee KH*, et al.* (2016) C9orf72 Dipeptide Repeats Impair the Assembly, Dynamics, and Function of Membrane-Less Organelles. *Cell* 167(3):774-788 e717.
35. Lin Y*, et al.* (2016) Toxic PR Poly-Dipeptides Encoded by the C9orf72 Repeat Expansion Target LC Domain Polymers. *Cell* 167(3):789-802 e712.
36. Mitrea DM*, et al.* (2016) Nucleophosmin integrates within the nucleolus via multi-modal interactions with proteins displaying R-rich linear motifs and rRNA. *Elife* 5.
37. Aumiller WM & Keating CD (2016) Phosphorylation-mediated RNA/peptide complex coacervation as a model for intracellular liquid organelles. *Nature Chemistry* 8(2):129-137.
38. Elbaum-Garfinkle S*, et al.* (2015) The disordered P granule protein LAF-1 drives phase separation into droplets with tunable viscosity and dynamics. *Proc Natl Acad Sci U S A* 112(23):7189-7194.
39. Ryan VH*, et al.* (2018) Mechanistic View of hnRNPA2 Low-Complexity Domain Structure, Interactions, and Phase Separation Altered by Mutation and Arginine Methylation. *Mol Cell* 69(3):465-479 e467.
40. Nott TJ*, et al.* (2015) Phase transition of a disordered nuage protein generates environmentally responsive membraneless organelles. *Mol Cell* 57(5):936-947.
41. Bogaert E*, et al.* (2018) Molecular Dissection of FUS Points at Synergistic Effect of Low-Complexity Domains in Toxicity. *Cell Rep* 24(3):529-537 e524.
42. Mori K*, et al.* (2013) The C9orf72 GGGGCC repeat is translated into aggregating dipeptide-repeat proteins in FTLD/ALS. *Science* 339(6125):1335-1338.
43. Ash PE*, et al.* (2013) Unconventional translation of C9ORF72 GGGGCC expansion generates insoluble polypeptides specific to c9FTD/ALS. *Neuron* 77(4):639-646.
44. Zu T*, et al.* (2013) RAN proteins and RNA foci from antisense transcripts in C9ORF72 ALS and frontotemporal dementia. *Proc Natl Acad Sci U S A* 110(51):E4968-4977.
45. Gallivan JP & Dougherty DA (1999) Cation-pi interactions in structural biology. *Proceedings of the National Academy of Sciences USA* 96(17):9459-9464.
46. Pak CW*, et al.* (2016) Sequence Determinants of Intracellular Phase Separation by Complex Coacervation of a Disordered Protein. *Mol Cell* 63(1):72-85.
47. Aumiller WM, Cakmak FP, Davis BW, & Keating CD (2016) RNA-Based Coacervates as a Model for Membraneless Organelles: Formation, Properties, and Interfacial Liposome Assembly. *Langmuir* 32(39):10042-10053.
48. Seol Y, Skinner GM, Visscher K, Buhot A, & Halperin A (2007) Stretching of homopolymeric RNA reveals single-stranded helices and base-stacking. *Phys Rev Lett* 98(15).
49. Petrovic AG & Polavarapu PL (2008) The quadruplex-duplex structural transition of polyriboguanylic acid. *J Phys Chem B* 112(7):2245-2254.

50. Sciortino F, Bansil R, Stanley HE, & Alstrom P (1993) Interference of Phase-Separation and Gelation - a Zeroth-Order Kinetic-Model. *Phys Rev E* 47(6):4615-4618.
51. Mascotti DP & Lohman TM (1997) Thermodynamics of Oligoarginines Binding to RNA and DNA. *Biochemistry* 36(23):7272-7279.
52. Priyakumar UD, Hyeon C, Thirumalai D, & MacKerell AD (2009) Urea Destabilizes RNA by Forming Stacking Interactions and Multiple Hydrogen Bonds with Nucleic Acid Bases. *J Am Chem Soc* 131(49):17759-17761.
53. Zaccarelli E, Lu PJ, Ciulla F, Weitz DA, & Sciortino F (2008) Gelation as arrested phase separation in short-ranged attractive colloid-polymer mixtures. *J Phys-Condens Mat* 20(49).
54. Wei MT*, et al.* (2017) Phase behaviour of disordered proteins underlying low density and high permeability of liquid organelles. *Nat Chem* 9(11):1118-1125.
55. Gallivan JP & Dougherty DA (1999) Cation-pi interactions in structural biology. *P Natl Acad Sci USA* 96(17):9459-9464.
56. Burley SK & Petsko GA (1988) Weakly polar interactions in proteins. *Advances in protein chemistry* 39:125-189.
57. Wang J*, et al.* (2018) A Molecular Grammar Governing the Driving Forces for Phase Separation of Prion-like RNA Binding Proteins. *Cell* 174(3):688-699. e616.
58. Brady JP*, et al.* (2017) Structural and hydrodynamic properties of an intrinsically disordered region of a germ cell-specific protein on phase separation. *Proc Natl Acad Sci U S A* 114(39):E8194-E8203.
59. Tanaka H, Araki T, Koyama T, & Nishikawa Y (2005) Universality of viscoelastic phase separation in soft matter. *Journal of Physics: Condensed Matter* 17(45):S3195.
60. Burke KA, Janke AM, Rhine CL, & Fawzi NL (2015) Residue-by-Residue View of In Vitro FUS Granules that Bind the C-Terminal Domain of RNA Polymerase II. *Mol Cell* 60(2):231-241.
61. Lam YW, Lamond AI, Mann M, & Andersen JS (2007) Analysis of nucleolar protein dynamics reveals the nuclear degradation of ribosomal proteins. *Curr Biol* 17(9):749-760.
62. Hubstenberger A*, et al.* (2017) P-Body Purification Reveals the Condensation of Repressed mRNA Regulons. *Mol Cell* 68(1):144-157 e145.
63. Simon JR, Carroll NJ, Rubinstein M, Chilkoti A, & Lopez GP (2017) Programming molecular self-assembly of intrinsically disordered proteins containing sequences of low complexity. *Nat Chem* 9(6):509-515.
64. Schmidt HB & Rohatgi R (2016) In Vivo Formation of Vacuolated Multi-phase Compartments Lacking Membranes. *Cell reports* 16(5):1228-1236.
65. Maharana S*, et al.* (2018) RNA buffers the phase separation behavior of prion-like RNA binding proteins. *Science*.
66. Langdon EM*, et al.* (2018) mRNA structure determines specificity of a polyQ-driven phase separation. *Science* 360(6391):922-927.
67. Seeman NC & Sleiman HF (2017) DNA nanotechnology. *Nature Reviews Materials* 3:17068.
68. Han D*, et al.* (2017) Single-stranded DNA and RNA origami. *Science* 358(6369).
69. Geary C, Rothemund PW, & Andersen ES (2014) RNA nanostructures. A single-stranded architecture for cotranscriptional folding of RNA nanostructures. *Science* 345(6198):799-804.
70. Liu K*, et al.* (2015) Solvent-free Liquid Crystals and Liquids from DNA. *Chem-Eur J* 21(13):4898-4903.
71. Lundin KE, Gissberg O, & Smith CI (2015) Oligonucleotide Therapies: The Past and the Present. *Hum Gene Ther* 26(8):475-485.
72. Stein CA & Castanotto D (2017) FDA-Approved Oligonucleotide Therapies in 2017. *Mol Ther* 25(5):1069-1075.

73. Lu SW, *et al.* (2010) Arginine-Rich Intracellular Delivery Peptides Synchronously Deliver Covalently and Noncovalently Linked Proteins into Plant Cells. *J Agr Food Chem* 58(4):2288-2294.
74. Liu BR, Lin MD, Chiang HJ, & Lee HJ (2012) Arginine-rich cell-penetrating peptides deliver gene into living human cells. *Gene* 505(1):37-45.
75. Schmidt N, Mishra A, Lai GH, & Wong GCL (2010) Arginine-rich cell-penetrating peptides. *Febs Lett* 584(9):1806-1813.
76. Cordier C, *et al.* (2014) Delivery of Antisense Peptide Nucleic Acids to Cells by Conjugation with Small Arginine-Rich Cell-Penetrating Peptide (R/W)9. *Plos One* 9(8).
77. Boeynaems S, De Decker M, Tompa P, & Van Den Bosch L (2017) Arginine-rich Peptides Can Actively Mediate Liquid-liquid Phase Separation. *Bio-protocol* 7(17).
78. Brangwynne CP, Mitchison TJ, & Hyman AA (2011) Active liquid-like behavior of nucleoli determines their size and shape in Xenopus laevis oocytes. *Proc Natl Acad Sci U S A* 108(11):4334-4339.
79. Le Gros MA, *et al.* (2011) Visualizing Sub-cellular Organization Using Soft X-ray Tomography. *Comprehensive Biophysics, Vol 2: Biophysical Techniques for Characterization of Cells*:90-110.
80. Le Gros MA, *et al.* (2014) Biological soft X-ray tomography on beamline 2.1 at the Advanced Light Source. *J Synchrotron Radiat* 21:1370-1377.
81. Le Gros MA, *et al.* (2016) Soft X-Ray Tomography Reveals Gradual Chromatin Compaction and Reorganization during Neurogenesis In Vivo. *Cell reports* 17(8):2125-2136.
82. Feric M, *et al.* (2016) Coexisting liquid phases underlie nucleolar subcompartments. *Cell* 165(7):1686-1697.
83. Fichthorn KA & Weinberg WH (1991) Theoretical foundations of dynamical Monte Carlo simulations. *The Journal of chemical physics* 95(2):1090-1096.
84. Bieler NS, Knowles TP, Frenkel D, & Vácha R (2012) Connecting macroscopic observables and microscopic assembly events in amyloid formation using coarse grained simulations. *PLoS computational biology* 8(10):e1002692.
85. Šarić A, *et al.* (2016) Physical determinants of the self-replication of protein fibrils. *Nat. Phys.* 12(9):874-880.
86. Šarić A, Chebaro YC, Knowles TPJ, & Frenkel D (2014) Crucial role of nonspecific interactions in amyloid nucleation. *Proceedings of the National Academy of Sciences* 111(50):17869-17874.
87. McGibbon RT, *et al.* (2015) MDTraj: a modern, open library for the analysis of molecular dynamics trajectories. *Biophys. J.* 109(8):1528-1532.
88. Humphrey W, Dalke A, & Schulten K (1996) VMD: Visual molecular dynamics. *J. Mol. Graph. Model.* 14(1):33-38, 27-38.